Salt Transport Regimes Caused by Tidal and Subtidal Processes in Narrow Estuaries

Dijkstra, Yoeri M.; Schuttelaars, Henk M.; Kranenburg, Wouter M.

DOI
10.1029/2021JC018391

Publication date
2022

Document Version
Final published version

Published in
Journal of Geophysical Research: Oceans

Citation (APA)
Dijkstra, Y. M., Schuttelaars, H. M., & Kranenburg, W. M. (2022). Salt Transport Regimes Caused by Tidal and Subtidal Processes in Narrow Estuaries. *Journal of Geophysical Research: Oceans*, *127*(12), Article e2021JC018391. https://doi.org/10.1029/2021JC018391

JGR Oceans

RESEARCH ARTICLE
10.1029/2021JC018391

Key Points:

- Using a systematic model analysis, we identified seven mechanistic regimes that can dominate the salt balance in narrow estuaries
- We developed a model-based classification of the seven regimes as a function of four dimensionless parameters
- We identified a new regime, where salt import is dominated by correlations in the depth-averaged tidal flow and salinity

Supporting Information:

Supporting Information may be found in the online version of this article.

Correspondence to:

Y. M. Dijkstra,
y.m.dijkstra@tudelft.nl

Citation:

Dijkstra, Y. M., Schuttelaars, H. M., & Kranenburg, W. M. (2022). Salt transport regimes caused by tidal and subtidal processes in narrow estuaries. *Journal of Geophysical Research: Oceans*, *127*, e2021JC018391. https://doi.org/10.1029/2021JC018391

Received 27 DEC 2021
Accepted 9 NOV 2022

Author Contributions:

Conceptualization: Yoeri M. Dijkstra, Henk M. Schuttelaars
Data curation: Wouter M. Kranenburg
Formal analysis: Yoeri M. Dijkstra
Funding acquisition: Henk M. Schuttelaars
Investigation: Yoeri M. Dijkstra
Methodology: Yoeri M. Dijkstra, Henk M. Schuttelaars
Project Administration: Henk M. Schuttelaars
Resources: Wouter M. Kranenburg
Software: Yoeri M. Dijkstra
Validation: Yoeri M. Dijkstra, Wouter M. Kranenburg

Salt Transport Regimes Caused by Tidal and Subtidal Processes in Narrow Estuaries

Yoeri M. Dijkstra[1], Henk M. Schuttelaars[1], and Wouter M. Kranenburg[2,3]

[1]Delft Institute of Applied Mathematics, Delft University of Technology, Delft, The Netherlands, [2]Deltares, Marine and Coastal Systems Unit, Delft, The Netherlands, [3]Faculty of Civil Engineering and Geosciences, Delft University of Technology, Delft, The Netherlands

Abstract Tidally averaged transport of salt in estuaries is controlled by various subtidal and tidal processes. In this study, we show the relative importance of various subtidal and tidal transport processes in a width-averaged sense. This is done for a large range of forcing and geometric parameters, which describe well-mixed to salt wedge estuaries. To this end, we develop a width-averaged process-based model aimed at conducting and analyzing a large number of experiments (~40,000). We find that the salt transport is dominated by one of seven salt transport balances, or *regimes*. Four of these regimes are dominated by subtidal processes, while the other three are dominated by tidal processes. Which regime occurs in a part of an estuary depends on four dimensionless parameters, representing local geometry, and forcing conditions. One of the regimes features salt import by correlations between the depth-averaged tidal velocity and salinity. While this mechanism was previously only associated with along-channel geometric variations, we find it can also be a dominant mechanism in a significant part of the parameter space due to river-induced tidal asymmetry, independent of river geometry. We apply our classification to a case study of part of the Dutch Rhine delta and compare to decomposition results of a fully realistic three-dimensional model. We find the estuary features two regimes, with import dominated by subtidal shear transport in the seaward part of the estuary and by depth-averaged tidal correlations in the landward part of the estuary.

Plain Language Summary The distribution of salt water in an estuary is controlled by the balance of various processes related to tidal flows and subtidal processes. We investigate which processes are most important in determining this salt distribution for a wide range of parameter configurations including depth, river discharge, and tidal flow, thereby representing many types of estuaries found around the World. To this end, we develop a width-averaged model that is specifically suitable for investigating a large number of configurations (~40,000). We find that different processes are important for different parameter configurations, resulting in seven possible balances of processes, or regimes. The regime found in each part of an estuary is determined by four dimensionless parameters. We apply our classification to part of the Dutch Rhine delta and show that this estuary features two regimes depending on the location along the estuary.

1. Introduction

The distribution of salt in an estuary is continuously adapting to the balance between the various processes that import and export salt. On a tidally averaged time scale, these transport processes are usually categorized as being a consequence of covariance between subtidal flows and subtidal salinity (hereafter "subtidal processes") or as the covariance of tidally varying flow and salinity (hereafter "tidal processes"). Analysis of salt transport balances in various estuaries has shown that either subtidal or tidal processes can be dominant depending on the estuary, the location in the estuary, and on forcing parameters, including river discharge and tidal amplitude (e.g., Aristizábal & Chant, 2013; Bellafiore et al., 2021; Bowen & Geyer, 2003; Fischer, 1972; Wang et al., 2015). The various subtidal and tidal transport processes each have a different sensitivity to changing forcing parameters (e.g., tides and river discharge) and geometry (depth or width). Hence, to understand how the salt intrusion and stratification in an estuary change with changing parameters, it is important to understand which mechanisms dominate the salt transport. However, there is currently no comprehensive theory that describes the relative importance of subtidal and tidal processes as a function of the estuarine parameters, such as depth, width, river run-off, or tides for general estuaries. This work contributes to such theory focusing on width-averaged processes.

Visualization: Yoeri M. Dijkstra
Writing – original draft: Yoeri M. Dijkstra
Writing – review & editing: Henk M. Schuttelaars, Wouter M. Kranenburg

Most studies that describe the sensitivity of salt importing processes to changes in parameters have focused on either subtidal or tidal processes in a certain type of estuary. For example, focusing on the width-averaged dynamics, the subtidal models of Hansen and Rattray (1965), Chatwin (1976), and MacCready (2004) apply to partially mixed estuaries and demonstrate the importance of subtidal transport due to gravitational circulation. The two-layer models of, e.g., Schijf and Schönfeld (1953) and Armi (1986) apply to salt wedge estuaries and show that subtidal momentum advection and gravitational circulation are both important. Concerning tidal width-averaged processes, Bowden (1965), Chatwin (1975), Larsen (1977), and Wei et al. (2016) focus on well-mixed estuaries and discuss the transport due to the correlation between vertical shear of the tidal velocity and tidally varying salinity. Other tidal salt transport mechanisms include those due to the interaction between the main channel and shallow flanks or side-embayments, called "tidal trapping" (MacVean & Stacey, 2011; Okubo, 1973), temporally varying mixing in tidally varying salt wedge estuaries (Geyer & Farmer, 1989), and rapid changes in bathymetry and geometry (Geyer & Ralston, 2015). We refer to Fischer et al. (1979) and Geyer and Ralston (2011) for reviews of these and other processes.

The aim of this study is to construct a classification of salt transport balances, or *regimes*, which shows the relative importance of width-averaged subtidal and tidal salt transport processes across a large range of parameters. These include forcing parameters (i.e., related to river discharge and tide) and geometric parameters (i.e., depth and width) representative of narrow estuaries ranging from well-mixed to salt wedge. We further focus on single channel estuaries without side-embayments and only gradually varying bathymetry. Further important assumptions include temporally and spatially uniform mixing parameters and negligible surface elevation (i.e., rigid lid). The classification is derived from a systematic analysis of the results of a model that solves for the conservation laws for water motion and salinity. This work thereby extends that of Dijkstra and Schuttelaars (2021) (*hereafter DS21*), who constructed such a classification focusing only on width-averaged subtidal processes.

The forcing and geometric parameters usually vary strongly along an estuary and in time. Still, regions within an estuary and periods of time can typically be distinguished in which the tidal amplitude, river discharge, depth, and width are fairly constant. This allows for developing a classification that is representative of the local dynamics, i.e., dynamics in a part of an estuary during a certain period of time. We model this by assuming an infinitely long estuarine domain with uniform forcing and geometric parameters representing these local dynamics. The dominant transport processes in this domain are then assumed to be representative for the local dynamics. Resolving an entire estuary like this has the advantage over a local model (e.g., a 1D-vertical model such as Lange and Burchard (2019)) that the response of the along-channel salinity gradient to the forcing and geometry is fully resolved, not prescribed. We will apply this approach and verify our results by classifying the dominant salt transport balances along the Rotterdam Waterway-Nieuwe Maas River (RWW, part of the Rhine Delta, The Netherlands) by comparing our classification against results of a three-dimensional simulation model.

In Section 2, we first introduce the model equations, the dedicated solution procedure and the way the salt transport contributions are decomposed. Next, in Section 3, we present our classification, describe the identified regimes, and show the dependence of salt intrusion on the forcing and geometric parameters in each regime. The discussion in Section 4 presents the application to the RWW, a comparison of our classification to previous results, and an overview of processes that are not explicitly resolved. Finally, Section 5 summarizes the main findings.

2. Model

2.1. Model Equations

We develop a width-averaged model for water motion and salinity including both tidal and subtidal dynamics. As mentioned in Section 1, all forcing and geometric parameters are assumed constant in the along-channel direction. This also implies that the tidal velocity amplitude and phase are constant along the entire domain, so that the model does not resolve tidal propagation. This is done so that we can unambiguously speak of the effect caused by a tide of specific velocity amplitude and phase independent of estuary depth, length, or friction. The model is forced by a constant river discharge and constant depth-integrated M_2 tidal velocity. Overtides (M_4, M_6, etc.) are resolved but assumed to have no depth-integrated contribution.

We assume that the (tidal) surface variations are small compared to the depth (rigid lid assumption). Hence, the model domain is described by Cartesian coordinates with the vertical coordinate z from the flat bed $z = -H$ to a

fixed surface level at $z = 0$ and the along-channel coordinate x from the mouth at $x = 0$ to the upstream boundary at $x = L$. The length L is chosen much larger than the salt intrusion limit, such that it does not affect the results. Note here that our assumption of an along-channel constant tidal velocity amplitude and phase also means that the estuary length does not affect the tides.

The water motion is described by the width-averaged continuity and momentum equations. Effects of turbulence are parametrized by a constant (in time and space) vertical eddy viscosity A_v. We assume that A_v is an independent parameter, meaning that the results do not rely on a specific choice of turbulence model to determine A_v but require explicit input of A_v (e.g., from a simple closure, observations, or simulation models). We further assume hydrostatic pressure and include density effects in the pressure terms only (i.e., Boussinesq approximation). The density ρ is related linearly to salinity as $\rho = \rho_0(1 + \beta s)$, where ρ_0 is a reference density of 1,000 kg/m^3, $\beta = 7.6 \cdot 10^{-4}$ psu^{-1} and s is salinity. Under these assumptions, the model equations read as

$$u_x + w_z = 0 \tag{1a}$$

$$u_t + uu_x + wu_z = -g\zeta_x + g\beta \int_z^0 s_x \, dz' + A_v u_{zz} \tag{1b}$$

Here, u and w denote the width-averaged horizontal and vertical velocity components. The width-averaged surface gradient ζ_x strictly needs to be interpreted as a source of pressure due to the rigid lid assumption, whereas its effect on the surface elevation is ignored. Furthermore, g is the acceleration of gravity. Subscripts t, x, and z denote derivatives with respect to time and space. The boundary conditions are given by

$$A_v u_z = 0 \qquad \text{at } z = 0, \tag{1c}$$

$$A_v u_z = s_f u \qquad \text{at } z = -H, \tag{1d}$$

$$w = 0 \qquad \text{at } z = 0, \tag{1e}$$

$$w = 0 \qquad \text{at } z = -H, \tag{1f}$$

$$\frac{1}{H}\int_{-H}^0 u \, dz = -\mathcal{U}_r + \mathcal{U}_t \cos(\omega t) \qquad \text{at } x = L, \tag{1g}$$

$$u_t - g\zeta_x + A_v u_{zz} = 0 \qquad \text{at } x = L, \tag{1h}$$

Boundary condition (1c) represents a no-stress condition at the surface (i.e., no wind) and (1d) a partial slip condition at the bed, using a spatially and temporally constant friction coefficient s_f (in m/s). The third and fourth boundary conditions (1e) and (1f) prescribe no flux through the rigid surface and bed. Equation 1g describes the external forcing, consisting of a constant fresh water velocity $\mathcal{U}_r \geq 0$, and a constant-amplitude M_2 tidal velocity $\mathcal{U}_t \cos(\omega t)$, where $\mathcal{U}_t \geq 0$ is the depth-averaged tidal velocity amplitude, $\omega = 1.4 \cdot 10^{-4}$ s^{-1} is the angular frequency of the M_2 tide. Without loss of generality the phase is fixed at zero. Finally, Equation 1h describes that the velocity profile at $x = L$ satisfies conditions of horizontally uniform (tidal) flow. Note that integration of the continuity Equation 1a over the cross-section and using boundary conditions (1e) and (1g) we find that the cross-sectionally averaged velocity equals $-\mathcal{U}_r + \mathcal{U}_t \cos(\omega t)$ not only at $x = L$ but in the entire estuary.

The salinity is described by the conservation equation

$$s_t + us_x + ws_z = K_v s_{zz} + K_h s_{xx} \tag{2a}$$

where K_v and K_h are the vertical and horizontal eddy diffusivity. Like A_v, we assume that K_v and K_h are independent parameters, which are constant in space and time. We set the following boundary conditions:

$$K_v s_z = 0 \qquad \text{at } z = 0, \tag{2b}$$

$$K_v s_z = 0 \qquad \text{at } z = -H, \tag{2c}$$

$$s_t + us_x + ws_z = K_v s_{zz} \qquad \text{at } x = 0,\ z \in (-H, 0], \tag{2d}$$

$$\max_t s = s_{\text{sea}} \qquad \text{at } x = 0,\ z = -H, \tag{2e}$$

$$[s]_x = 0 \qquad \text{at } x = 0,\ z = -H, \tag{2f}$$

$$s = 0 \qquad \text{at } x = L, \tag{2g}$$

Table 1
Default Parameter and Numerical Settings, Including Ranges of Parameters Used for the Sensitivity Study

	Parameter	Meaning	Value
Physical	U_r	Cross-sectionally averaged river velocity	$5 \cdot 10^{-4}$–2.2 m/s
	U_t	Cross-sectionally averaged tidal velocity	0–1 m/s
	K_h	Horizontal dispersion parameter	25–500 m^2/s
	A_v	Vertical eddy viscosity	$3.5 \cdot 10^{-5}$–3 m^2/s
	H	Depth	20 m
	ω	M_2 angular frequency	$1.4 \cdot 10^{-4}$ s^{-1}
	s_{sea}	Maximum seaward salinity	30 psu
	σ_ρ	Prandtl-Schmidt number A_v/K_v	2.2
	R	Viscosity-bottom friction ratio	0.5
Numerical	M	Number of spectral components in the vertical	12
	q_{max}	Number of harmonic components	3
	j_{max}	Number of adaptively spaced grid cells	200

where $[\cdot]$ means taking the tidal variation (i.e., removing the subtidal component). Conditions (2b) and (2c) are no-flux conditions at the surface and bed. The boundary conditions at $x = 0$ are adapted from MacCready (2004) and DS21: Equation 2d describes that the salinity at $x = 0$ satisfies the salt balance without horizontal diffusivity. Equation 2e fixes the maximum salinity that occurs during a tidal cycle at the bed at the seaward boundary to the sea/ocean salinity s_{sea}. Equation 2f requires that tidal variations of salinity should have a vanishing horizontal gradient for all time. Finally, Equation 2g describes a vanishing salinity at the upstream boundary.

The model contains three parameters related to turbulence in a water column: A_v, K_v, and s_f. We choose to relate these parameters to each other, so only A_v is considered an input variable to the model. The constant eddy viscosity and vertical eddy diffusivity are related as $K_v = A_v/\sigma_\rho$ where, for simplicity, we choose a fixed Prandtl-Schmidt number $\sigma_\rho = 2.2$ (e.g., Ralston et al., 2008). The eddy viscosity and friction parameter s_f are related to each other in terms of a dimensionless parameter $R = \frac{A_v}{s_f H}$. We assume a fixed value $R = 0.5$ which is the best fit to typical boundary-layer solutions for barotropic flow in a $k - \varepsilon$ model (Dijkstra et al., 2017a). The results of this study do not essentially depend on the choices of σ_ρ and R, see also Section 4.2.

2.2. Solution Procedure

We look for dynamic equilibrium solutions of the model equations, i.e., solutions that are periodically varying with tidal and overtidal frequencies but not on a subtidal time scale. The solution procedure is tailored to find this dynamic equilibrium in an efficient way, so that a large number of simulations of high numerical accuracy can be performed in a short time. This procedure extends that of DS21 by including the effects of tidal motion. Details of the solution procedure can be found in Supporting Information. Here, we provide a summary of the essential steps.

First, we focus on the temporal and vertical structure of the flow and salinity. As the model is forced by an M_2 tidal constituent and a constant river discharge, the solution consists only of a subtidal component, the M_2 tide, and its overtides (M_4, M_6, …), which are created by nonlinear interactions. The temporal behavior of the various physical quantities is approximated by a truncated series of q_{max} harmonic components plus a subtidal component. The vertical structure of the flow and salinity is approximated by a truncated eigenfunction expansion, using $M + 1$ cosine functions. This approach has the advantage that the circulation and stratification can already be captured accurately by a small number of functions (i.e., here $M = 12$, see Table 1). The temporal structure of ζ_x and the temporal-vertical structure of u and s are thus approximated as

$$u(x,z,t) = \sum_{m=0}^{M}\sum_{q=0}^{q_{\max}} \left(\beta_{mq}^{R}(x)\cos(\omega_q t) + \beta_{mq}^{I}(x)\sin(\omega_q t)\right)\cos(\lambda_m z) \tag{3a}$$

$$s(x,z,t) = \sum_{m=0}^{M}\sum_{q=0}^{q_{\max}} \left(\alpha_{mq}^{R}(x)\cos(\omega_q t) + \alpha_{mq}^{I}(x)\sin(\omega_q t)\right)\cos(\mu_m z) \tag{3b}$$

$$\zeta_x(x,t) = \sum_{q=0}^{q_{\max}} \zeta_q^{R}(x)\cos(q\omega t) + \zeta_q^{I}(x)\sin(q\omega t) \tag{3c}$$

Here, $\cos(\lambda_m z)$ and $\cos(\mu_m z)$ are the eigenfunctions and λ_m and μ_m are the eigenvalues chosen so that the eigenfunctions satisfy the vertical boundary conditions (1c) and (1d), (2b) and (2c) (see Supporting Information for the associated eigenvalue problem). Furthermore, ω_q denotes the angular frequency of the qth tidal component, with $q = 0$ the subtidal component (i.e., $\omega_0 = 0$). The vertical velocity w is obtained using the continuity Equation 1a and the expression for u.

We substitute the expansions for u, s, and ζ_x in the model equations, resulting in a set of $(2M + 1)(2q_{\max} + 1)$ equations for the unknown coefficient functions $\alpha_{mq}^{R}(x)$, $\alpha_{mq}^{I}(x)$, $\beta_{mq}^{R}(x)$, $\beta_{mq}^{I}(x)$, $\zeta_q^{R}(x)$, $\zeta_q^{I}(x)$, which depend on the along-channel coordinate. This system of equations is discretized using a second-order accurate finite volume method on a grid with $j_{\max} + 1$ grid points. The spacing between the grid points is adapted in such a way that the highest resolution is located in the region with the largest along-channel salinity gradient. The total system of equations consists of $(2M + 1)(2q_{\max} + 1)(j_{\max} + 1)$ nonlinear algebraic equations. This system is solved using a Newton-Raphson solver. For highly frictional situations (A_v large), the equations are nearly linear and this solver converges fast from any initial guess. When friction is weaker, the solutions are obtained using a continuation procedure, i.e., gradually decreasing A_v from one computation to the next and using the result of each computation as the initial guess for the next. The grid spacing is adapted based on the salinity gradient in this initial guess. This way, the solver converges within a few iterations.

2.3. Controlling Dimensionless Parameters

The model contains seven independent variables H, $\mathcal{U}_i$, $\mathcal{U}_r$, ω, s_{sea}, A_v, and K_h, two parameters that are assumed to be constant $R = 0.5$, $\sigma_\rho = 2.2$ (see above for motivation of these numbers), and two fundamental constants g and β. In order to reduce the number of variables, we rewrite the model equations to a dimensionless system and

F_r	Estuarine Froude number	$\frac{\mathcal{U}_r}{c_I}$
F_t	Tidal Froude number	$\frac{\mathcal{U}_t}{c_I}$
Ra	Estuarine Rayleigh number	$\frac{c_I^2 H^2}{A_v K_h}$
St	Stokes number	$\frac{A_v}{\omega H^2}$

consider the dimensionless parameters controlling it. As derived in Section 2 in Supporting Information S1, this reduces the independent variables to the following four dimensionless parameters:

where $c_I = \sqrt{\beta s_{\text{sea}} g H}$ is a measure for the internal wave speed of the fastest internal wave (e.g., MacCready, 2004). The estuarine Froude number F_r and Rayleigh number Ra are measures for the river-induced velocity and the reciprocal of mixing. These numbers also appear in subtidal models (see e.g., Hansen & Rattray, 1965; Guha & Lawrence, 2013, DS21). The tide additionally adds a tidal Froude number F_t (e.g., Geyer, 2010), which is the ratio of the tidal velocity amplitude and c_I, and the Stokes number (e.g., Souza, 2013), which is the ratio of a time scale for the water column to fully mix and the tidal time scale.

One of the important output parameters of the model is the salt intrusion length L_s, here defined as the distance from the mouth to the point where the bottom salinity equals 1 psu (see also DS21). The salt intrusion is

made dimensionless by scaling. The length scale used for this scaling is not important; it simply determines the magnitude of the dimensionless length scale. Here, we choose to use a dispersive length scale K_h/c_I, i.e., $\mathcal{L}_s = \frac{L_s c_I}{K_h}$ (see also DS21). Being a dependent parameter, the dimensionless salt intrusion length $\mathcal{L}_s$ may be expressed as some nonlinear function of the four independent parameters and the two chosen constants R and σ_ρ, i.e.

$$\mathcal{L}_s = f\left(F_r, F_t, Ra, St; \sigma_\rho, R\right) \tag{4}$$

2.4. Analysis of the Salt Transport

Transport of salt is analyzed by considering the depth-averaged, time-averaged salinity equation in equilibrium (e.g., Hansen & Rattray, 1965). Using our assumptions of constant depth and prescribed tides, this is obtained by integrating the salinity Equation 2a over depth, time averaging, and applying continuity (Equation 1a). This result reads as

$$T = \frac{1}{H}\left\langle \int_{-H}^{0} us - K_h s_x \, dz \right\rangle = 0 \tag{5}$$

where $\langle\cdot\rangle$ denotes averaging over a tidal cycle.

To disentangle the various contributions to this transport balance, we first follow the approach of Fischer (1976). That is, we write the velocity and salinity as a subtidal part, u_0, s_0, and tidally varying part, u_1, s_1 containing all resolved tidal harmonics. Next, each of these components is decomposed into its depth-mean $\bar{u}_i$, $\bar{s}_i$ $(i = 0, 1)$, and depth variation u_i', s_i', such that $\overline{u_i'} = 0$, $\overline{s_i'} = 0$. Thus, the velocity and salinity are written as

$$u = \bar{u}_0 + \bar{u}_1 + u_0' + u_1' \tag{6a}$$

$$s = \bar{s}_0 + \bar{s}_1 + s_0' + s_1' \tag{6b}$$

The transport balance (Equation 5) can then be rewritten as

$$T = \underbrace{\bar{u}_0\bar{s}_0}_{\substack{\text{subtidal}\\ \text{depth-averaged}\\ \text{transport}}} + \underbrace{\langle\bar{u}_1\bar{s}_1\rangle}_{\substack{\text{tidally correlated}\\ \text{depth-averaged}\\ \text{transport}}} + \underbrace{\overline{u_0's_0'}}_{\substack{\text{subtidal}\\ \text{shear}\\ \text{transport}}} + \underbrace{\left\langle\overline{u_1's_1'}\right\rangle}_{\substack{\text{tidally correlated}\\ \text{shear}\\ \text{transport}}} \underbrace{-K_h\bar{s}_{0,x}}_{\substack{\text{dispersive}\\ \text{transport}}} = 0 \tag{7}$$

Similar decompositions as in the above transport balance have been applied to analyze observations and models (e.g., Aristizábal & Chant, 2013; Bellafiore et al., 2021; Lerczak et al., 2006), although in many instances the transport by tidal depth-averaged correlations $\langle\bar{u}_1\bar{s}_1\rangle$ and tidal shear correlations $\langle\overline{u_1's_1'}\rangle$ are merged and the dispersive transport is not considered.

To more explicitly relate the decomposition above to the underlying physical mechanisms, the transport balance is further decomposed. We distinguish contributions by the *river discharge* (u_{riv}, s_{riv}), *barotropic tidal forcing* (u_{tide}, s_{tide}), *baroclinic pressure* (u_{gc}, s_{gc}), *momentum advection* (u_{adv}, s_{adv}), and *horizontal dispersion* $\left(s_{K_h}\right)$. These contributions are determined from a decomposition of the momentum Equation 1b, boundary condition (Equation 1g) and the salinity Equation 2a and is such that the sum of all contributions equals the total velocity and salinity. The decomposition is mathematically described by the following equations (terms in red mark the differences between the equations)

$$\begin{cases} u_{t,\mathrm{riv}} - g\zeta_{x,\mathrm{riv}} - A_v u_{zz,\mathrm{riv}} = 0, \\ \dfrac{1}{H}\int_{-H}^{0} u_{\mathrm{riv}}\, dz = -\mathcal{U}_r \qquad \text{at } x = L, \end{cases} \quad \text{(river)} \tag{8a}$$

$$\begin{cases} u_{t,\mathrm{tide}} - g\zeta_{x,\mathrm{tide}} - A_v u_{zz,\mathrm{tide}} = 0, \\ \dfrac{1}{H}\int_{-H}^{0} u_{\mathrm{tide}}\, dz = \mathcal{U}_t \cos(\omega t) \qquad \text{at } x = L, \end{cases} \quad \text{(tide)} \tag{8b}$$

$$\begin{cases} u_{t,\mathrm{gc}} - g\zeta_{x,\mathrm{gc}} - A_v u_{zz,\mathrm{gc}} = g\beta\int_{z}^{0} s_x\, dz', \\ \dfrac{1}{H}\int_{-H}^{0} u_{\mathrm{gc}}\, dz = 0 \qquad \text{at } x = L, \end{cases} \quad \text{(baroclinic pressure)} \tag{8c}$$

$$\begin{cases} u_{t,\mathrm{adv}} - g\zeta_{x,\mathrm{adv}} - A_v u_{zz,\mathrm{adv}} = -(uu_x + wu_z). \\ \dfrac{1}{H}\int_{-H}^{0} u_{\mathrm{adv}}\, dz = 0 \qquad \text{at } x = L, \end{cases} \quad \text{(momentum advection)} \tag{8d}$$

$$s_{t,\mathrm{riv}} - K_v s_{zz,\mathrm{riv}} = -(u_{\mathrm{riv}} s_x + w_{\mathrm{riv}} s_z), \quad \text{(river)} \tag{8e}$$

$$s_{t,\mathrm{tide}} - K_v s_{zz,\mathrm{tide}} = -(u_{\mathrm{tide}} s_x + w_{\mathrm{tide}} s_z), \quad \text{(tide)} \tag{8f}$$

$$s_{t,\mathrm{gc}} - K_v s_{zz,\mathrm{gc}} = -(u_{\mathrm{gc}} s_x + w_{\mathrm{gc}} s_z), \quad \text{(baroclinic pressure)} \tag{8g}$$

$$s_{t,\mathrm{adv}} - K_v s_{zz,\mathrm{adv}} = -(u_{\mathrm{adv}} s_x + w_{\mathrm{adv}} s_z), \quad \text{(momentum advection)} \tag{8h}$$

$$s_{t,K_h} - K_v s_{zz,K_h} = K_h s_{xx}, \quad \text{(horizontal dispersion)} \tag{8i}$$

These decompositions are computed in a postprocessing step as Equations 8c–8i require the solution u and s. For the velocity, we observe that the depth-averaged parts of u_{gc} and u_{adv} are zero. The salinity components are determined up to some constant. Hence, this provides a decomposition of the salinity shear, while there is no decomposition of the depth-averaged salinity. We may thus summarize the obtained components as

$\bar{u}_0$	$\bar{u}_{0,\mathrm{riv}}$	$\bar{s}_0$	No decomposition
$\bar{u}_1$	$\bar{u}_{1,\mathrm{tide}}$	$\bar{s}_1$	No decomposition
u'_0	$u'_{0,\mathrm{riv}}, u'_{0,\mathrm{gc}}, u'_{0,\mathrm{adv}}$	s'_0	$s'_{0,\mathrm{riv}}, s'_{0,\mathrm{tide}}, s'_{0,\mathrm{gc}}, s'_{0,\mathrm{adv}}, s'_{0,\mathrm{Kh}}$
u'_1	$u'_{1,\mathrm{tide}}, u'_{1,\mathrm{gc}}, u'_{1,\mathrm{adv}}$	s'_1	$s'_{1,\mathrm{riv}}, s'_{1,\mathrm{tide}}, s'_{1,\mathrm{gc}}, s'_{1,\mathrm{adv}}, s'_{1,\mathrm{Kh}}$

Taking all correlations of these decomposed velocity and salinity contributions in the transport Equation 5 results in a total of 33 physical mechanisms that transport salt. This number of contributions may seem too much to aid intuitive interpretation. However, it will turn out in the next section that only a few of these physical mechanisms are sufficient to understand the dominant balance and resulting salinity distribution. Hence, this decomposition does offer a useful framework for interpreting the results.

2.5. Model Experiments

In order to gain insight into the entire parameter space, the model is run for a large number of different settings of the four dimensionless parameters F_r, F_t, Ra, and $StRa$. This is done by varying the corresponding dimension-carrying model input parameters $\mathcal{U}_r$, $\mathcal{U}_t$, A_v, and K_h. The ranges of these parameters as well as the values of the other parameters are listed in Table 1. The experiments are carried out using a continuation approach (cf. Section 2.2), i.e., by keeping values of $\mathcal{U}_r$, $\mathcal{U}_t$, and K_h constant and gradually decreasing A_v and repeating this for other values of $\mathcal{U}_r$, $\mathcal{U}_t$, and K_h. Over 40,000 model experiments have been carried out to sample the complete parameter space.

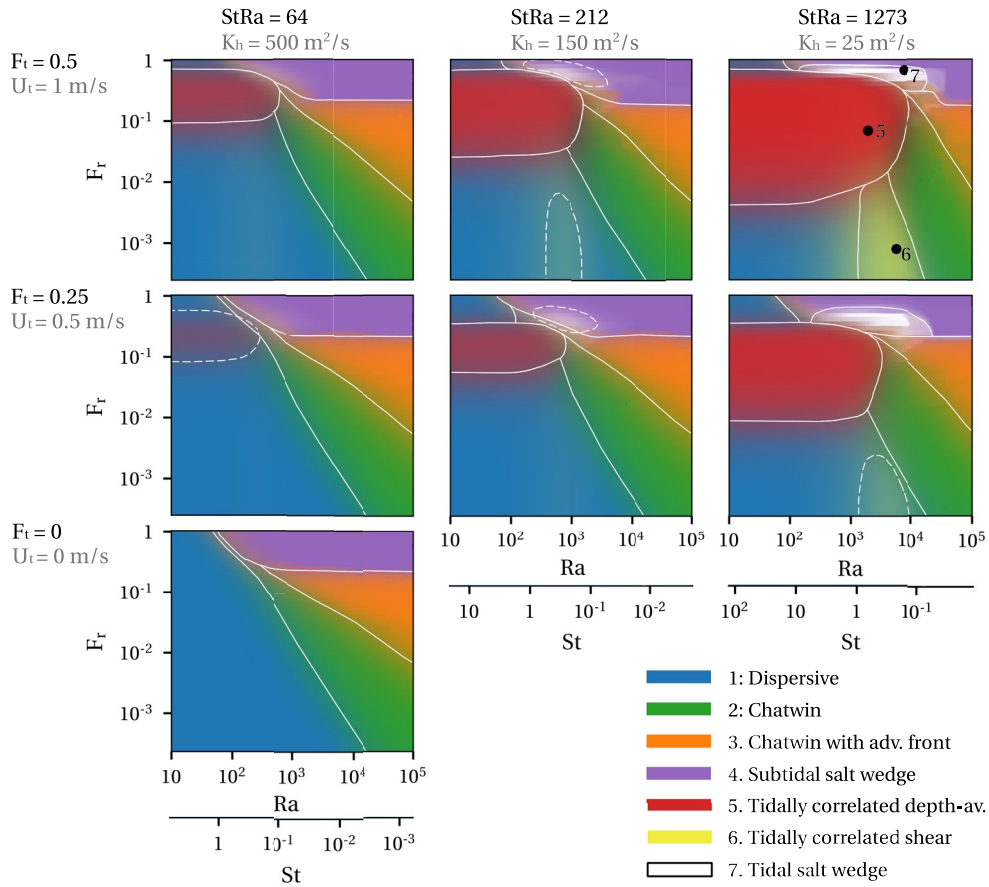

Figure 1. The seven regimes (colors) as a function of the four dimensionless parameters F_t, F_r, *Ra*, and *St*. Each panel has a different constant value of F_t and *StRa*, while the axes in each panel represent varying F_r (vertical axis) and *Ra* and *St* (horizontal axis, corresponding to changing A_v). White lines indicate the transitions between regimes, white dashed lines indicate a balance that is not dominant but contributes at least 20% to the total salt transport balance. The black dots in the upper-right panel mark the cases that are studied in Sections 3.3–3.5.

3. Results

We show the identified regimes in Section 3.1 and the corresponding stratification and salt intrusion in Section 3.2. This is then used to choose several specific parameter settings for which we analyze the water motion, salinity, and transport in more detail in Sections 3.3–3.5.

3.1. Regimes in Parameter Space

We systematically examined the salt transport processes in each of the model experiments. From this analysis, we identified seven distinct balances of salt transport mechanisms, called *regimes*. The precise algorithmic procedure for defining these regimes is provided in Section 3 in Supporting Information S1. The occurrence of the seven regimes in the parameter space is visualized in Figure 1. Each panel in the figure shows regimes indicated by different colors as a function of F_r (vertical axis) and *Ra*, *St*. Note that *Ra* and *St* change simultaneously on the horizontal axis, which corresponds to changing A_v. The various panels represent different combinations of F_t and the product $StRa = \frac{c_t^2}{\omega K_h}$. Moving from the lower panels up, F_t increases (i.e., tidal velocity increases). Moving from the left panels to the right, *StRa* increases (i.e., K_h decreases). In each model experiment, between 80% and 100% (in most experiments well over 90%) of the salt transport is described by the processes in either one regime or a combination of these regimes. The white lines in the figure separate regions where the mechanisms from one regime are more important than those in each of the other regimes. Close to these white lines, the colors in the figure blend continuously into each other. Here, one regime still dominates but 1–3 other regimes also play a

role in the salt balance. White dashed lines are added in some of the panels where certain regimes never occur as most important, but do have a share in the salt balance of >20%.

Of the seven regimes, the first four regimes were already identified in the subtidal study of DS21. We provide a short summary of these regimes here and refer to DS21 for an elaborate discussion. The four subtidal regimes are

1. *Dispersive Regime.* Governed by a balance between salt transport due to background dispersion (through K_h) and river-induced flushing. The background dispersion parametrizes various mechanisms including lateral variations of the flow and salinity and effects of temporally varying eddy viscosity.
2. *Chatwin Regime*. Regime as described by Chatwin (1976), which is a balance between the transport due to subtidal shear by gravitational circulation $\langle \overline{u'_{0,\mathrm{gc}} s'_{0,\mathrm{gc}}} \rangle$ and river-induced flushing.
3. *Chatwin Regime With Advection Dominated Front.* This is a transition regime that is characterized by satisfying the Chatwin regime when considering regions close to the mouth. When considering the regions near the salt intrusion limit, transport due to subtidal shear by momentum advection becomes dominant, i.e., $\langle \overline{u'_{0,\mathrm{adv}} s'_{0,\mathrm{gc}}} \rangle$, $\langle \overline{u'_{0,\mathrm{gc}} s'_{0,\mathrm{adv}}} \rangle$, and $\langle \overline{u'_{0,\mathrm{adv}} s'_{0,\mathrm{adv}}} \rangle$. This leads to the formation of a front-like salinity profile locally.
4. *Subtidal Salt Wedge Regime*. Transport due to subtidal shear by momentum advection dominates in the entire estuary. The solution for the salinity resembles a stationary salt wedge and is well described by two-layer theory (e.g., Schijf & Schönfeld, 1953).

   Naturally, these four regimes are the only regimes occurring when there are no tides (i.e., bottom panel of Figure 1). The subtidal regimes also take a prominent place in the parameter space when tides are included. Besides these four dominantly subtidal regimes, we identify three regimes where tidal processes dominate. These are summarized here and discussed in more detail in the next sections.

5. *Tidally Correlated Depth-Averaged Transport Regime*. A balance between transport due to tidally correlated depth-averaged transport $\langle \overline{u}_1 \overline{s}_1 \rangle$ and river-induced flushing. In literature, tidally correlated depth-averaged transport has only been associated with the interchange of salt between a main channel and side-embayments and shallows (i.e., "tidal trapping") (Fischer et al., 1979; MacVean & Stacey, 2011; Okubo, 1973) or other geometric features, such as shoals or river junctions (Dronkers & van de Kreeke, 1986). However, none of these geometric features are explicitly included in this study. We will show that presence of both a tidal flow and significant river flow can also cause a strong tidally correlated depth-averaged transport, independent of variations in bathymetry or geometry.
6. *Tidally Correlated Shear Transport Regime*. Balance between transport due to tidally correlated shear transport specifically by the term $\langle \overline{u'_{1,\mathrm{tide}} s'_{1,\mathrm{tide}}} \rangle$ and river-induced flushing. Here, $u'_{1,\mathrm{tide}}$ is the vertical shear in the tidal velocity and $s'_{1,\mathrm{tide}}$ is the vertical salinity shear induced by the tidal velocity shear. This regime has been discussed from a theoretical perspective by several authors, including Bowden (1965), Chatwin (1975), Larsen (1977), Watson (1983), Ou et al. (2000), and Wei et al. (2016).
7. *Tidal Salt Wedge Regime*. The net transports by subtidal processes and tidal correlations related to momentum advection dominate in the entire estuary. Hence, besides the mechanisms in regime 4, we find an important role for the transport contributions $\langle \overline{u'_{1,\mathrm{adv}} s'_{1,\mathrm{gc}}} \rangle$, $\langle \overline{u'_{1,\mathrm{gc}} s'_{1,\mathrm{adv}}} \rangle$, and $\langle \overline{u'_{1,\mathrm{adv}} s'_{1,\mathrm{adv}}} \rangle$.

In Figure 1, we see a prominent place for the tidally correlated depth-averaged transport regime (regime 5, red color). The tidally correlated shear transport regime (regime 6, yellow) is only dominant in a part of the parameter space in the top-right panel (large tide, small K_h). In two other panels, this regime does make contribution of >20% in part of the parameter space (indicated by the dashed white lines). Finally, the tidal salt wedge regime only dominates a part of the parameter space in the right column (small K_h) and makes a contribution of over 20% in the middle column.

3.2. Stratification and Salt Intrusion

In this section, we investigate the characteristics of the regimes in terms of stratification and dimensionless salt intrusion length. Here, the dimensionless salt intrusion length is a global quantity, assuming that the entire estuary can be characterized by the same value of the (dimensionless) parameters. Figure 2 presents the maximum (in time and space) top-to-bottom stratification, tidally averaged dimensionless salt intrusion length $\langle \mathcal{L}_s \rangle$, and the ratio of the tidal variation of L_s and the subtidal L_s. This is done for the case without tides (corresponding to the bottom-left panel in Figure 1) and with $\mathcal{U}_t = 1$ m/s and $StRa = 1{,}273$ (corresponding to the top-right panel in Figure 1). The white lines again indicate the boundaries between the regimes and were copied from the respective

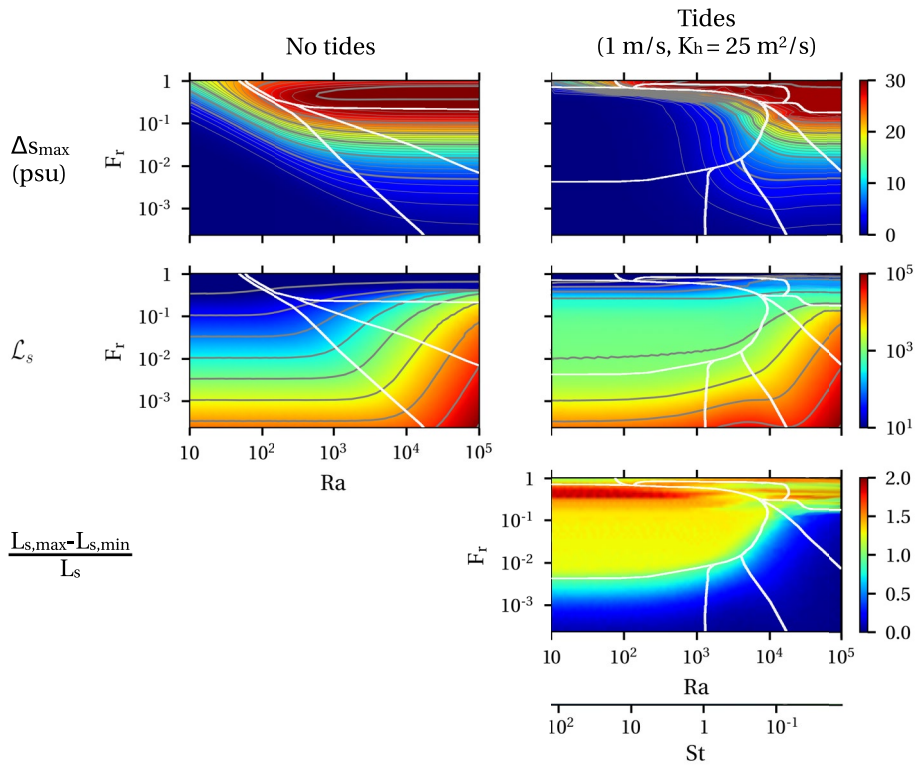

Figure 2. Maximum subtidal top-bottom stratification (in psu; upper panels), dimensionless salt intrusion (middle panels) and relative tidal salt intrusion (lower panel) for the case without tides (left) and with 1 m/s tides (right). The white lines indicate the transitions between regimes from Figure 1.

panels in Figure 1. Concentrating on the first row, which plots stratification, the case without tides shows that stratification increases with increasing F_r and increasing *Ra* (i.e., decreasing *St* or decreasing mixing). As concluded by DS21, stratification is not uniquely related to the regime, except for regime 4, which is always strongly stratified. Adding tides (top-right panel in Figure 2) we again do not find a unique relation between stratification and regime. The main difference with the case without tide is found for intermediate F_r and small *Ra*. Comparison to Figure 1 shows this part of the parameter space is dominated by the tidally correlated depth-averaged transport regime (regime 5). In most of this regime, the stratification is small; a few psu. However, substantial stratification may occur in the transition zone of this regime to the Chatwin and salt wedge regimes.

The second row in Figure 2 shows the dimensionless salt intrusion length $\mathcal{L}_s$. In both the subtidal and tidal cases, $\mathcal{L}_s$ increases with decreasing F_r. For small *Ra* (large mixing), estuaries are in regime 1 or 5 and $\mathcal{L}_s$ is insensitive to changing *Ra*. For larger *Ra*, the regimes change and $\mathcal{L}_s$ increases for increasing *Ra*. The value of $\mathcal{L}_s$ shows little relation to the regimes 1, 2, 3, and 6. In the tidally correlated depth-averaged transport regime (regime 5), $\mathcal{L}_s$ is fairly independent of both F_r and *Ra*. In the salt wedge regimes 4 and 7, the salt intrusion length is always relatively small. This does not imply that estuaries with a salt distribution looking like a salt wedge necessarily have a small salt intrusion length. Salt wedge-like salt distributions occur in a broad transition region from regimes 3 and 5 to regimes 4 and 7 and hence can also feature larger salt intrusion length. In contrast, our definition of the salt wedge regimes is very strict; requiring the corresponding transport mechanisms are dominant in the entire estuary. Comparing the subtidal and tidal cases, the addition of tides mainly leads to a difference in salt intrusion in regime 5. This will be explained in more detail in Section 3.3.

The third row in Figure 2 shows the ratio of the tidal excursion of the salt intrusion and the subtidal salt intrusion. As the tidal variation of the salt intrusion scales with the tidal excursion length, this ratio is small when the subtidal salt intrusion greatly exceeds the tidal excursion length. From the figure, it is clear that this is characteristic for the subtidal dispersive and Chatwin regimes (regimes 1, 2, and 3) as well as the tidally correlated shear transport regime (regime 6). On the other hand, the tidal variation of the salt intrusion length and subtidal salt

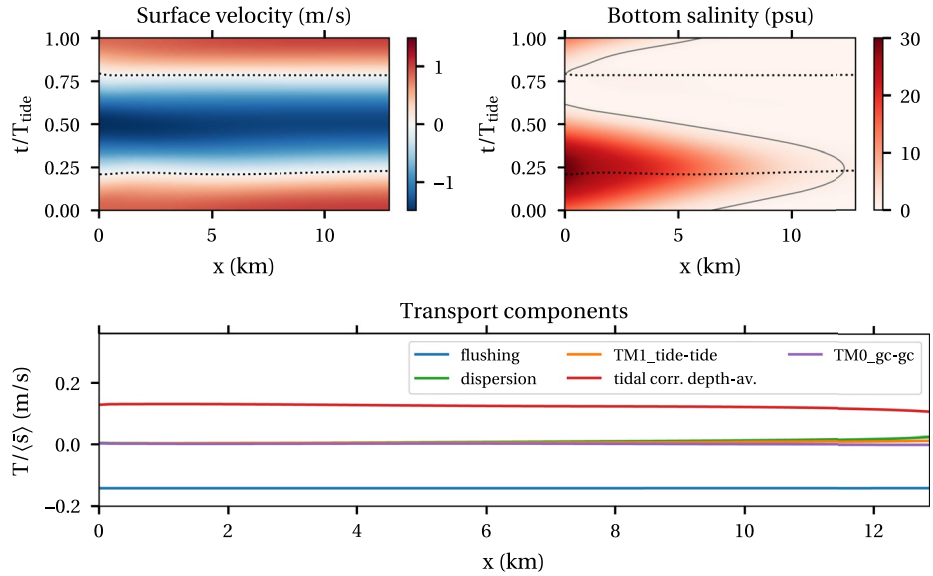

Figure 3. Example representing the tidally correlated depth-averaged transport regime (see mark 5 in Figure 1). Model results are shown for the surface velocity, bottom salinity, and the tidally averaged salt transport divided by the subtidal depth-averaged salinity. For the transport contributions in the lower panel TM0 and TM1 denote subtidal and tidal covariance, respectively, and the terms following it denote the contributions to u and s (see Section 2.4).

intrusion length are of the same order of magnitude in the subtidal and tidal salt wedge regimes (regimes 4 and 7) and the tidally correlated depth-averaged transport regime (regime 5). This implies that the salinity is almost entirely flushed from the estuary during part of the tide in the cases where these regimes dominate the entire estuary.

3.3. Tidally Correlated Depth-Averaged Transport Regime

The first tide-dominated regime we discuss is the tidally correlated depth-averaged transport regime. This regime can be described by the following simplified form of the Fischer decomposition (Equation 7):

$$\underbrace{\bar{u}_{0,\mathrm{riv}}\bar{s}_0}_{\substack{\text{transport by}\\ \text{mean flow}}} + \underbrace{\langle \bar{u}_{1,\mathrm{tide}}\bar{s}_1 \rangle}_{\substack{\text{tidal}\\ \text{mean transport}}} = 0 \tag{9}$$

Figure 3 shows an example of a case from the tidally correlated depth-averaged transport regime using $F_r = 7 \cdot 10^{-2}$, $F_t = 0.5$, $Ra = 1{,}940$, and $StRa = 1{,}273$ (marked by 5 in Figure 1). The top panels show the surface velocity and bottom salinity as a function of x and t, which are representative of the entire water column as the salinity is well-mixed and there is little exchange flow. The gray dashed lines indicate the time of slack water. The surface velocity shows an almost perfectly symmetric tide, affected only slightly by the river discharge (visible as slack water occurs at $t/T_{\mathrm{tide}} < 0.25$ and $t/T_{\mathrm{tide}} > 0.75$). Subtidal salinity decays in the along-channel direction but there is strong temporal variation over the tide, so that the salt is flushed out of the estuary during part of the tidal cycle. Maximum salt intrusion coincides with high water slack, while minimum salt intrusion occurs before low water slack. In terms of tidal components, the phase difference between the M_2 tidal salinity and tidal velocity is ~80°. The higher harmonics, M_4 and M_6, of the salinity signal are the reason that maximum salt intrusion still occurs at high water slack. The bottom panel in the figure shows the most important contributions to the salt transport per m^2 cross-sectional area and divided by the depth-averaged and time-averaged salinity. Here, TM0 and TM1 denote subtidal and tidal covariance, respectively, and the terms following it denote the contributions to u and s (see Section 2.4). The subtidal salt import is entirely governed by tidally correlated depth-averaged transport (red line), balanced by river-induced export (blue line), confirming Equation 9 is a good approximation.

Many theoretical analyses of tidal salt transport conclude that tidally correlated depth-averaged transport is (approximately) zero in along-channel uniform estuaries with a tide-dominated current (e.g., Chatwin, 1975). This is because $\bar{u}$ and $\bar{s}$ are 90° out of phase in that case. Okubo (1973) and MacVean and Stacey (2011) show that tidally correlated depth-averaged transport can be caused by tidal trapping: the interaction between the main channel and shallower sides or side-embayments, which change the phase difference between the depth-averaged tidal velocity and salinity (also see Fischer et al., 1979). Dronkers and van de Kreeke (1986) argue that also other geometric features, such as shoals, river branching, and the transition to the open sea may be causes for such a phase difference. They furthermore use the term "nonlocal" transport, as they show the tidal depth-averaged transport depends on the variations of $\bar{u}$ and $\bar{s}$ over the tidal excursion length. All above-mentioned authors assume that the river flow may be neglected compared to the tidal flow. As our case has along-channel uniform parameters, one would conclude from literature that tidally correlated depth-averaged transport should vanish.

To understand why we nevertheless find a big tidally correlated depth-averaged transport, we look closer at the analytical solution of the approximate transport balance Equation 9. This is used together with a simplified depth-averaged balance for the M_2 salinity component and our definitions $\bar{u}_0 = \mathcal{U}_r$ and $\bar{u}_1 = \mathcal{U}_t \cos(\omega t)$. The equations considered are

$$-\mathcal{U}_r \bar{s}_{0,x} + \langle \mathcal{U}_t \cos(\omega t) \bar{s}_{1,x} \rangle = 0 \tag{10a}$$

$$\bar{s}_{1,t} - \mathcal{U}_r \bar{s}_{1,x} + \mathcal{U}_t \cos(\omega t) \bar{s}_{0,x} = 0 \tag{10b}$$

where $\bar{s}_0$ still denotes the depth-averaged subtidal salinity and $\bar{s}_1$ now specifically denotes the depth-averaged M_2 component of the salinity. The derivation and solution procedure for this simplified system are presented in Appendix A. The resulting subtidal salinity follows an exponential profile $\bar{s}_0 = s_{\text{sea}} e^{-\lambda x}$ with a decay rate

$$\lambda = \frac{\omega}{\sqrt{\frac{1}{2}\mathcal{U}_t^2 - \mathcal{U}_r^2}}, \qquad (\text{assuming } \mathcal{U}_r^2 < \frac{1}{2}\mathcal{U}_t^2) \tag{11a}$$

$$\approx \sqrt{2}\frac{\omega}{\mathcal{U}_t} \qquad \text{if } \mathcal{U}_r \ll \mathcal{U}_t \tag{11b}$$

For river velocities much smaller than the tidal amplitude, Equation 11b, the salt intrusion length scales with the tidal excursion length. As we defined the salt intrusion length as the distance to the 1 psu line, we obtain $L_s = \ln(s_{\text{sea}})/\lambda$, or (assuming $s_{\text{sea}} = 30$ psu)

$$L_s \approx 2.4\frac{\mathcal{U}_t}{\omega} \tag{12}$$

In terms of dimensionless numbers, the dimensionless salt intrusion length $\mathcal{L}_s$ scales with $F_t StRa$. As the subtidal salinity can be approximately be described by an exponential profile, it can also be considered as the solution from a 1D dispersion law (i.e., following $D_{\text{tide-depth-averaged}} \bar{s}_{0,x} + \mathcal{U}_r \bar{s}_0 = 0$) with dispersion parameter

$$D_{\text{tide-depth-averaged}} \sim \frac{\mathcal{U}_r \mathcal{U}_t}{\omega} \text{ (assuming } \mathcal{U}_r \ll \mathcal{U}_t) \tag{13}$$

In dimensionless numbers: $\frac{D_{\text{tide-depth-averaged}}}{\kappa_h} \sim F_r F_t StRa$.

The above reasoning requires no geometric features to create a phase difference between $\bar{u}$ and $\bar{s}$, as suggested necessary by the literature. Also, the above reasoning does not depend on the seaward boundary condition, which was used only to set the value of $\bar{s}_0$ at $x = 0$, so the effects of exchange between the estuary and the sea are not needed as well. The reason that the tidally correlated depth-averaged transport nevertheless occurs in this case, is the presence of both a tidal and river flow. The nonzero river discharge results in a phase difference between velocity and salinity smaller than 90°. The finding that river discharge can induce tidally correlated depth-averaged transport is new.

This finding also explains why the tidally correlated depth-averaged transport regime disappears for small river discharges. It is expected that a depth-averaged M_4 overtide can play a similar role as river discharge leading to a

significant tidal depth-averaged transport, so it is likely that this regime occurs in estuaries with a small river flow but strong overtides. Since we assumed a zero depth-averaged M_4 velocity, this is not explicitly resolved here.

These analytical estimates explain our findings in Figures 1 and 2. First, the expression for the salt intrusion length agrees with the observation from Figure 2 that the salt intrusion length in the tidally correlated depth-averaged transport regime is almost constant under varying F_r and Ra, St if $StRa$ and F_t are kept constant. Small variations of the salt intrusion length nevertheless occur, as the regimes gradually transition into each other. Second, we see from the figure that this regime disappears for high F_r, which is consistent with Equation 11a becoming invalid for $\mathcal{U}_r > \frac{1}{\sqrt{2}}\mathcal{U}_t$ as the simplified balance of Equation 9 has no solution in that case (i.e., import is insufficient to balance the large river-induced export). Third, the dimensionless dispersion coefficient associated with the tidally correlated depth-averaged transport increases with $\mathcal{F}_r$, $\mathcal{F}_t$, and $StRa$, while the dimensionless dispersion coefficient in the dispersive regime (regime 1) is a constant. Hence, the current regime dominates over the dispersive regime for large F_r, F_t, and $StRa$, as confirmed by Figure 1.

Only accounting for the subtidal and M_2 component is a coarse approximation. A much closer approximation is obtained when also taking into account the M_4 salinity component. The analytical solution procedure for the resulting system of equations is shown in Section 4 in Supporting Information S1. With this addition, the subtidal salt intrusion no longer follows an exponential profile and is therefore not precisely described by a dispersion law. Otherwise, all conclusions drawn above remain valid, and the salt intrusion length-scale derived above still provides a good approximation of the salt intrusion length. Section 4 in Supporting Information S1 also describes the effect of accounting for phase propagation of the tidal velocity $\mathcal{U}_t$, showing that this effect is typically negligible.

3.4. Tidally Correlated Shear Transport Regime

In the tidally correlated shear transport regime, salt is imported by the covariance of tidal velocity shear and tidal salinity shear and flushed out by the river discharge. Hence, the balance reduces to approximately

$$\underbrace{\bar{u}_{0,\mathrm{riv}}\bar{s}_0}_{\substack{\text{transport by}\\ \text{mean flow}}} + \underbrace{\overline{\langle u'_{1,\mathrm{tide}} s'_{1,\mathrm{tide}}\rangle}}_{\substack{\text{tidal}\\ \text{shear transport}}} = 0 \tag{14}$$

An example of the tidal shear dispersion regime is shown in Figure 4 using the parameter settings $F_r = 8 \cdot 10^{-4}$, $F_t = 0.5$, $Ra = 5{,}600$, and $StRa = 1{,}300$ (see 6 in Figure 1). As in the previous regime, the exchange flow is small and hence the surface velocity (top-left panel) shows an M_2 tide modulated by a small river discharge. The bottom salinity (top-right panel) is representative of the salinity in the water column as top-to-bottom stratification is smaller than 1 psu. It shows a dominantly subtidal salt intrusion with a small tidal modulation, where maximum salt intrusion occurs close to high water slack. The bottom panel shows two important processes for salt import: the tidally correlated shear transport (TM1_tide-tide) and dispersion, with the tidal shear transport about twice more important than dispersion in this case. This case is thus a combination of regimes 1 and 6, where regime 6 is most important.

The tidally correlated shear transport mechanism was first discussed by Bowden (1965) for the limit of large Stokes numbers and was generalized by, e.g., Holley et al. (1970), Chatwin (1975), Larsen (1977), Fischer et al. (1979), and Watson (1983) (see Chatwin and Allen (1985) for a review). Ou et al. (2000) discussed this mechanism on a sloping bed. McCarthy (1993) and Wei et al. (2016) provided the first analytical description of the above balance (14) appended with horizontal dispersive transport, but tidally correlated shear transport was never dominant in their case studies.

All the above authors have demonstrated that the tidally correlated shear transport can be approximated closely by a dispersion process. This dispersion process can be written as $\overline{\langle u'_{1,\mathrm{tide}} s'_{1,\mathrm{tide}}\rangle} = D_{\text{tide-tide}}\bar{s}_{x,0}$, where

$$D_{\text{tide-tide}} = \frac{\mathcal{U}_t^2 H^2}{A_v} F\left(St; \sigma_\rho, R\right) \tag{15}$$

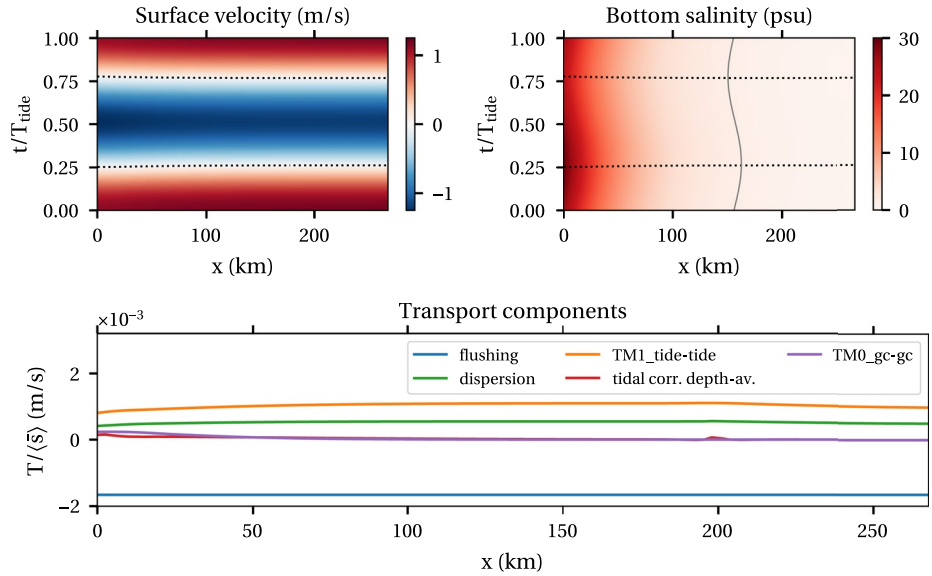

Figure 4. Example representing the tidally correlated shear transport regime (see mark 6 in Figure 1).

where F is some nonlinear function F that depends on the Stokes number $St = \frac{A_v}{\omega H^2}$, σ_ρ, and R. Wei et al. (2016) provide a closed-form expression for F for the case $\sigma_\rho = 1$. Figure 5 shows $D_{\text{tide-tide}}$ as function of A_ν for the parameter settings of the example in Figure 4 and two variations, with $H = 10$ m and $R = 0$ (i.e., representing a no-slip bottom boundary; cf. Fischer et al. (1979, Figure 7.4)). For the default settings (blue line), $D_{\text{tide-tide}}$ varies over >1 order of magnitude with its maximum occurring for intermediate values of A_ν. We may understand this physically as follows: for large values of A_ν (i.e., large St) the system is too strongly mixed to create substantial salinity shear, while for small A_ν (i.e., small St) the mixing is so small that the salinity shear cannot adjust to the tidal motion within the tidal period. As a result, the maximum tidally correlated shear transport occurs at intermediate A_ν (intermediate St). As this transport contribution scales with St, reducing H by a factor 2 (green line), means we find the maximum transport at a 4 times smaller A_ν, such that the maximum occurs for the same value of St. When changing the viscosity-friction ratio R to represent a no-slip condition (orange line), the tidally correlated shear transport increases significantly by over an order of magnitude.

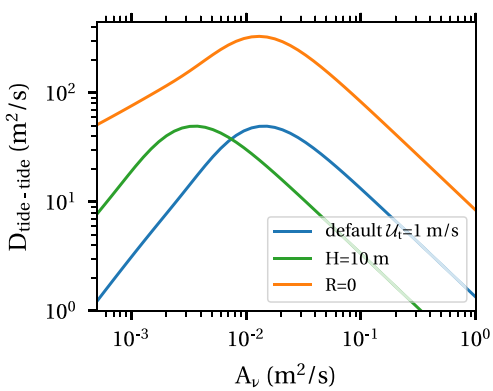

Figure 5. Equivalent dispersion parameter $D_{\text{tide-tide}}$ (Equation 15) for the tidally correlated shear transport as a function of the eddy viscosity A_ν for the default case (blue), a twice shallower case (green), and the default case with viscosity-friction ratio $R = 0$, representing a no-slip bottom boundary (orange).

3.5. Tidal Salt Wedge Regime

The tidal salt wedge regime is exemplified in Figure 6, showing results using $F_r = 0.73$, $F_t = 0.5$, $Ra = 7{,}600$, and $StRa = 1{,}300$ (see 7 in Figure 1). Here, and everywhere where this regime dominates, $F_r \geq F_t$, so that the depth-averaged velocity is always negative. The bottom velocity (top-left panel) however is positive during the flood tide due to the strong estuarine circulation. Salt intrusion correspondingly is greatest during the flood tide ($0 < t/T_{\text{tide}} < 0.25$ and $0.75 < t/T_{\text{tide}} < 1$), with the maximum intrusion occurring almost at peak flood ($t/T_{\text{tide}} = 0$). Salt is flushed out of the estuary during the ebb tide, where it is important to note that salt water is assumed to remain close to the estuary mouth with our boundary conditions. Nevertheless, salt water only returns when the tide is close to peak flood. The bottom panel of Figure 6 shows the governing transport processes are related to the baroclinic pressure and momentum advection. Throughout the estuary subtidal processes (indicated by TM0) are as important as the tidal correlations (indicated by TM1).

Analytical or otherwise highly simplified analysis of the tidal salt wedge seems restricted. Jay and Smith (1990) analyze a tidal two-layer model, but assume $F_r \ll F_t$ and neglect momentum advection at the leading order. Given our results, this is clearly not the appropriate scaling for this regime. Geyer

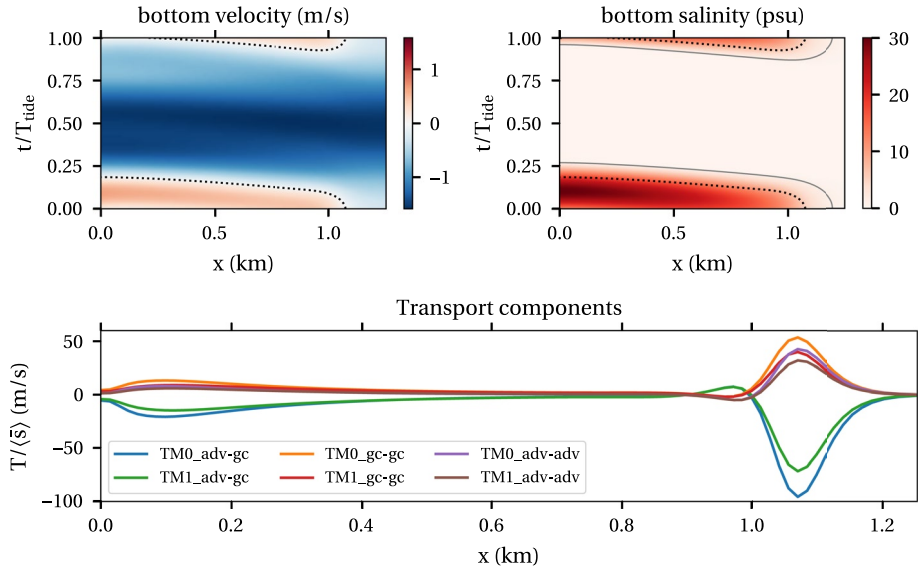

Figure 6. Example representing the tidal salt wedge regime (see mark 7 in Figure 1). Model results are shown for the near-bed velocity, bottom salinity and the tidally averaged salt transport divided by the subtidal depth-averaged salinity.

and Farmer (1989) and Geyer and Ralston (2011) offer an alternative approach by studying the tidal salt wedge assuming the flow and salinity are quasi-stationary at each moment during the tide. This assumption seems a reasonable, yet coarse approximation for the case studied in Figure 6: the maximum salt intrusion occurs at peak flood consistent with a quasi-stationary view, but salt intrusion is not symmetric around peak flood, indicating salinity cannot fully adjust to instantaneous flow conditions. The main result of quasi-stationary theory states that a salt wedge cannot persist if the internal flow becomes critical, i.e., when the velocity in one layer exceeds the internal wave speed c_I. The exact time at which the flow becomes internally critical depends on the precise definition used for c_I and the layer velocity. Estimating these quantities for our case study indeed shows internally critical flow during most of the ebb phase. Geyer and Farmer (1989) also describe intense mixing in the process of breaking down the salt wedge. This requires mixing parameters that vary in time and space, which is not explicitly accounted for in our model. So, while this model captures some of the important characteristics of a salt wedge, likely not all important physical processes are described (also see Section 4.3).

4. Discussion

4.1. Case Study: The Rotterdam Waterway

Below we first apply our classification to the Rotterdam Waterway and compare the regimes found with transports in a simulation model. Next, we provide some general guidelines and lessons-learned for application to other estuaries.

Application to the Rotterdam Waterway, we apply our classification to determine the regimes in the RWW, which is a partially mixed to salt wedge estuary in the Dutch Rhine delta. We verify our results by comparing our classification against results of the 3D hydrostatic OSR model (abbreviation from Dutch meaning "operational flow model Rotterdam") of the lower Rhine-Meuse delta (Netherlands), developed and maintained by the Port of Rotterdam (see https://www.portofrotterdam.com/en/operational-information/hydrometeo-data for the operational results and Kranenburg et al. (2015) for a description and model evaluation). The OSR model is built within SIMONA, an established modeling suite that has been in use as official software for the Dutch Directorate-General for Public Works and Water Management since the early 1990s (De Goede, 2020). We focus on the part of the delta indicated by the red line in Figure 7a following the RWW from the North Sea, ~10 km downstream of Hook of Holland (km 0) to the junction with the Hollandse IJssel (km 37). This part of the delta is a fairly narrow, almost prismatic and highly engineered estuary in the Rhine-Meuse delta, which forms the entrance channel to the Port of Rotterdam. We consider one spring-neap cycle in the period from 17 to 31 August 2003. During this time, the upstream discharge of the Rhine at the Dutch border at Lobith was low: 900–1,000 m^3/s.

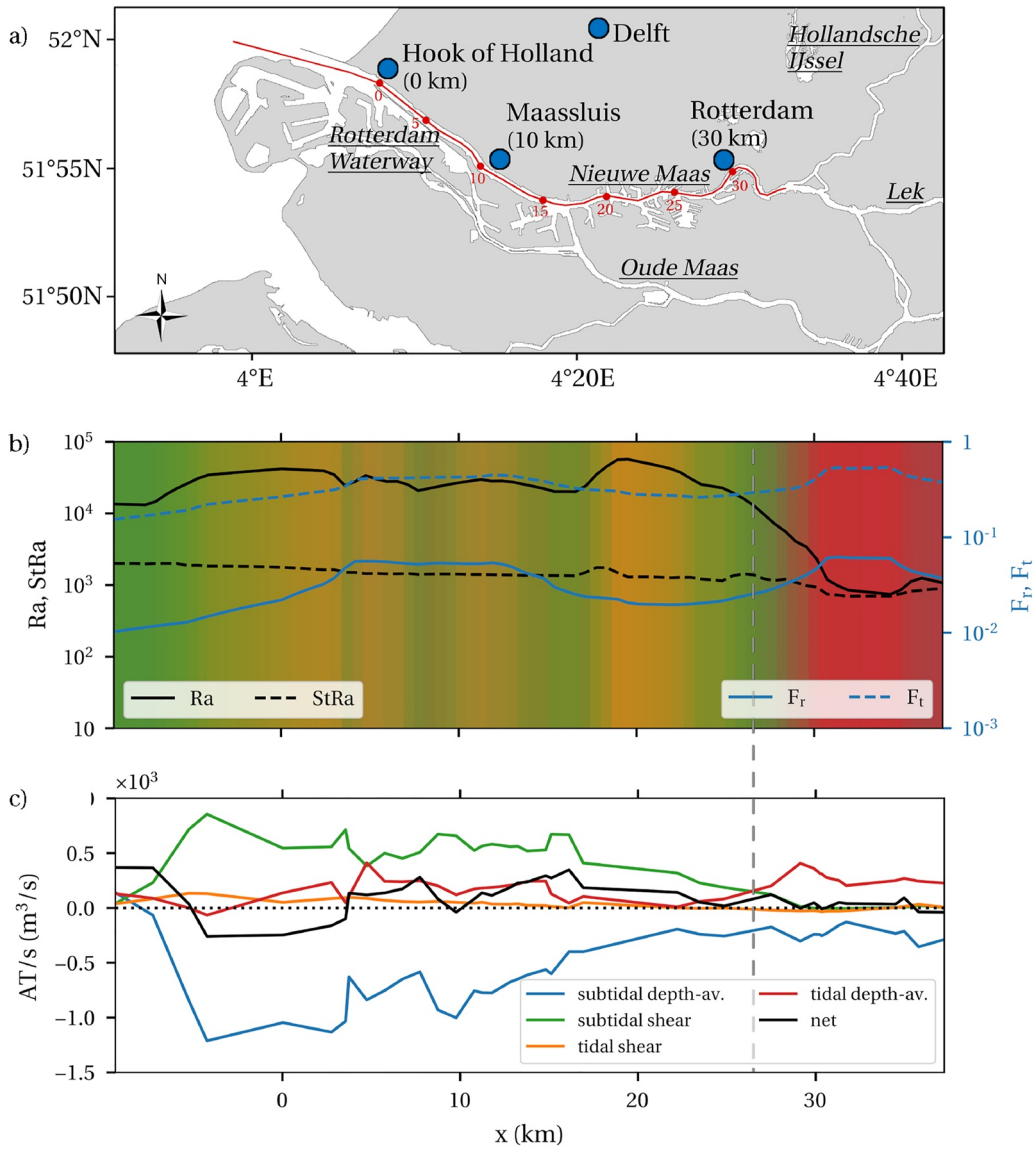

Figure 7. (a) Rotterdam Waterway-Nieuwe Maas river (RWW) in the Dutch Rhine delta. The red line indicates the along-channel section of the model domain that is represented in panels (b) and (c). (b) Spring-neap averaged values of the dimensionless parameters (lines) along the RWW during low discharge conditions on 17–31 August 2003 as estimated from the three-dimensional OSR model. Colors indicate the corresponding regime corresponding to colors in Figure 1 with green and orange the Chatwin regimes (regimes 2 and 3) and red the tidally correlated depth-averaged transport regime (regime 5). (c) Direct decomposition of the salt transport from the OSR model by Kranenburg and Van der Kaaij (2019) plotted as transport integrated over the cross-sectional area (A) and divided by the mean salinity. The vertical dashed gray line indicates the location of the transition between regimes according to this decomposition.

To establish a classification for the RWW, we first determined the values of the dimensionless numbers F_r, F_t, Ra, and St as a function of the along-channel coordinate using the OSR model input and output (spring-neap averaged H, $\mathcal{U}_t$, $\mathcal{U}_r$) from 41 locations along the thalweg. Additionally, we used $K_h = 20$ m^2/s and checked that the regimes obtained are not sensitive to this choice (see below for more information). The eddy viscosity was estimated based on a reconstruction that used the velocity and salinity from the OSR model in a damping function-type closure as in Pacanowski and Philander (1981) and Wei et al. (2021). See Supporting Information S1 for details. The resulting values of the dimensionless numbers are plotted in Figure 7b. For each along-channel position, we look up the regime from our classification for the local combination of the dimensionless parameters. In other words, the local parameters are translated into an infinitely long estuary with uniform parameters, the salt transport is computed and the resulting dominant processes are assumed to also be dominant locally in the estuary (see

also Section 1). We have recomputed the classification as in Figure 1 using $\sigma_\rho = 0.7$ as this is the value used in the OSR model, instead of $\sigma_\rho = 2.2$; this results only in minor quantitative changes while the classification diagram of Figure 1 is qualitatively the same.

The regime as a function of along-channel distance is indicated using the colors in Figure 7b, where colors match those in Figure 1. Between the mouth and km 26, we alternatingly find regimes 2 (green) and 3 (orange), which are both Chatwin regimes where subtidal shear due to gravitational circulation balances river-induced export. Between km 26 and 30, we find a transition to regime 5 (red), the tidally correlated depth-averaged regime, which is dominant in the upstream part of the estuary.

We compare our classification to a direct decomposition of the OSR model results made by Kranenburg and Van der Kaaij (2019) and Kranenburg et al. (2022), decomposing into the four contributions given in Equation 7, i.e., subtidal and tidally correlated depth-averaged and shear transports (excluding dispersive transport). The result of their decomposition is shown in Figure 7c. Note the net transport (black line) is not completely zero, meaning that the spring-neap averaged transports are not entirely in dynamic equilibrium. They find the transport by the subtidal shear contribution is dominant for $x < 26.5$ km and transport by the tidally correlated depth-averaged transport dominates for $x > 26.5$ km. This transition point is indicated by the gray-dotted line. Even though the three-dimensional OSR model explicitly accounts for many more processes related to turbulence and lateral correlations, as well as tidal trapping in the many harbor basins in the RWW, the results of the decomposition match our classification in 7b. Only the exact transition point is shifted between the two methods, as the red color appears only a few km ahead of the 26.5 km point (gray-dotted line) in Figure 7b. This case study demonstrates how our classification may be used for the classification of real estuaries and can qualitatively identify not only a regime, but also the transition of one regime into another within one estuary. The method can further be used to classify estuaries under various forcing conditions (e.g., high and low discharge) or compare different estuaries to each other.

Guidelines for application to other estuaries, the current study is aimed at identifying the regimes and their occurrence in the parameter space, not as a foolproof classification tool. In applying the classification, we found that it is especially difficult to determine the parameters K_h and A_ν, which results in some degree of arbitrariness.

To select K_h one could start with a small value, so the estuary is not in or near regime 1. The exact value of K_h will then not affect the results, as dispersive transport is not important. Any small change in K_h will affect Ra and $StRa$ in such a way that the final classification and salt intrusion length remains the same. If the observed and modeled salinity gradient or stratification are not similar, one could consider to increase K_h (possibly as a function of x) so that dispersive transport becomes important and creates a better match between modeled and observed salinity.

The vertical eddy viscosity A_ν can be determined to some extent on the basis of models or observations. While this worked in our application with a simple turbulence model, this is not infallible as A_ν parametrizes effects of vertical, lateral, and temporal variations in mixing. The match between observed and modeled salinity gradients and stratification may be used here as well as a motivation to change A_ν.

4.2. Comparison With Other Studies

Many of the regimes discussed in this study have been covered in previous studies focusing either on specific mechanisms or analysis of numerical models or observations. We look closer at the part of the parameter space covered by several of these studies in Table 2. Focusing first on general mechanistic studies, the regimes described by several studies is indicated by an x. The subtidal regimes 1, 2, 3, and 4 as well as the tidal correlations regimes 6 and 7 (to some extent) have been covered, although no study covers all of these regimes at once. This study for the first time describes the tidally correlated depth-averaged transport regime resulting from a river-induced asymmetry. Earlier studies only attributed this transport to geometric features of the estuary (see also Section 3.3).

Next concentrating on analysis methods for observations or complex numerical models, decomposition is usually done along the lines of Fischer (1976). A popular compact form of this decomposition used by, e.g., Bowen and Geyer (2003) and Lerczak et al. (2006) distinguishes between tidally correlated transport F_T and subtidal transport due to the exchange flow F_E. As shown in Table 2 dominance of either F_T or F_E may indicate dominance of multiple regimes. Dronkers and van de Kreeke (1986) chose a different compact form, distinguishing between tidally correlated depth-averaged transport (denoted by K_1, see Table 2) and all shear transport contributions (K_2).

Table 2
Selection of Other Studies Presenting Either Detailed Mechanistic Description or Decomposition Methods for Data or Complex Model Results and the Regimes That Are Described

		Regime						
	Study	1	2	3	4	5	6	7
Mechanistic	Schijf and Schönfeld (1953)				x			
	Hansen and Rattray (1965)	x	x					
	Chatwin (1976)		x					
	Geyer and Farmer (1989)				x			x
	MacCready (2004)	x	x					
	Wei et al. (2016)	x					x	
	Dijkstra and Schuttelaars (2021)	x	x	x	x			
Decomposition	Dronkers and van de Kreeke (1986)		K_2	K_2	K_2	K_1	K_2	K_2
	Lerczak et al. (2006)		F_E	F_E	F_E	F_T	F_T	F_T
	Garcia et al. (2021)		F_3	F_3	F_3	F_1	F_4	F_4

Note. Under "mechanistic," an x indicates that this regime is described by the respective study. Under "decomposition," the different terms correspond to the terms used in the respective studies (colors are used to emphasize the different terms), showing that different authors have made different groupings of regimes in their decompositions.

Recently, Kranenburg and Van der Kaaij (2019) and Garcia et al. (2021) combined the above two approaches and distinguished between tidally correlated depth-averaged transport (F_1, see Table 2), subtidal shear transport (F_3), and tidally correlated shear transport (F_4). More elaborate decompositions have been made by, e.g., Dyer (1974) and Hughes and Rattray (1980), adding transport related to fluctuations of the surface level and lateral correlations, which in our approach is partly parametrized by K_h. Concluding, while no decomposition method is able to uniquely identify each individual physical process or regime, they do all distinguish collections of dominant processes or regimes. This can be used to estimate approximate parameter dependencies and is greatly helpful for understanding results of realistic models and observations. It also provides a useful tool for model reduction to operational one-dimensional models (Kranenburg et al., 2016).

4.3. Unresolved Dynamics

Salt transport in real estuaries is greatly complex. In this study, some of this complexity is parametrized, meaning that some of the salt transport is not explicitly accounted for. In this section, we discuss how our assumptions relate to missing salt transport processes and how our assumptions affect the interpretation of the classification. First, the model is width-averaged and hence the effect of any lateral variation in flow and salinity is parametrized in the dispersion parameter K_h. As Fischer et al. (1979) note, lateral correlations of velocity and salinity are dominant for the salt transport in quite a number of estuaries. Explicitly resolving the lateral dimension will likely result in a further specification of K_h and in new regimes that partly replace the dispersive regime 1.

Second, we assumed a tidally constant eddy viscosity. Most notably, this assumption does not account for the effect of tidal variations of stratification (or SIPS, Simpson et al., 1990) on the eddy viscosity. Adding SIPS-induced tidal variations of the eddy viscosity affects the stratification, phasing of the salinity relative to the velocity as well as the exchange flow through ESCO circulation (Dijkstra et al., 2017b), which can cause a significant additional salt transport. This could impact our classification in several ways. For example, Geyer and MacCready (2014) discuss the existence of an SIPS-dominated regime. Furthermore, the tidal salt wedge regime is usually described in literature in terms of variations in mixing over the tidal cycle (Geyer & Farmer, 1989), so including tidal variations of the eddy viscosity are expected to be important for an accurate description of this regime.

We treated the eddy viscosity and vertical and horizontal eddy diffusivity as independent parameters in our study. In reality, these parameters are not independent but depend strongly and nonlinearly on the flow and salinity through complicated turbulence closure models. This means that changes in, e.g., tidal velocity in an estuary will not only affect the parameter F_t but simultaneously affect Ra and St through the turbulence closure.

Three-dimensional models with advanced turbulence closures are therefore still necessary to determine how a change in estuarine parameters affects F_t, F_r, Ra, and St and hence the regimes in an estuary.

As discussed by, e.g., Dronkers and van de Kreeke (1986), geometric elements (e.g., shallows, branches, side-basins) are potential causes for additional salt transport. Nevertheless, from our application in Section 4.1, it seems that the geometric elements in the RWW do not need to be considered to determine the dominant salt transport process.

Finally, when considering variations on short temporal scales (i.e., shorter than the adjustment time of the estuary, e.g., see Kranenburg, 1986) the dynamic equilibrium described in this study may not be attained. Furthermore, the combination of adjustment on short temporal scales over bathymetric variations on short spatial length scales in the estuary has been associated with features such as frontogenesis (Geyer & Ralston, 2015), which is also not described by this study.

5. Conclusions

We have investigated the relative importance of various subtidal and tidally correlated contributions to the tidally averaged estuarine salt balance. We focused on a local description of the salt balance, so that all geometric and forcing parameters could be assumed along-channel uniform, while dynamically resolving the vertical and horizontal profiles of the salinity. This approach allowed us to express the salinity and salt intrusion as a function of four dimensionless parameters describing the geometric and forcing conditions in an estuary. By varying these four dimensionless parameters over several orders of magnitude in over 40,000 model experiments, a large estuarine parameter space was systematically explored.

The main new finding of this work is that the entire parameter space features seven balances of salt transport mechanisms, called regimes. Almost all essential transport processes in these regimes have been described individually in literature. However, the tidally correlated depth-averaged transport was previously only associated with tidal trapping or prominent geometric features. Here, we demonstrated for the first time that this regime can also occur due to tidal asymmetry, in our case caused by a significant river discharge. Assuming a straight uniform prismatic channel, we found an analytical estimate for the typical salt intrusion length in the regime where this transport dominates, which scales with the tidal excursion length.

Although application of our classification to real estuaries is not the main goal, as a verification we compared our classification to transport contributions identified in a realistic simulation model of the RWW. The classification qualitatively matches the results from the direct decomposition, also demonstrating the existence of the tidally correlated depth-averaged transport regime in the RWW upstream from km 26 during low discharge conditions. The classification elegantly shows how and why dominant physical mechanisms vary throughout a single estuary, vary between estuaries, and vary as a function of variable forcing conditions.

Appendix A: Analytical Solution for the Tidally Correlated Depth-Averaged Transport Balance

The tidally correlated depth-averaged transport balance can be approximated analytically. In this section, we show the simplest approximation that uses only information from the subtidal and M_2 tidal components and which yields easy analytical length-scale estimates. An extended approximation also using the M_4 tide but otherwise following a similar derivation is presented in Section 3.1 in Supporting Information S1. Furthermore, the reasoning is extended to include the effects of adding phase propagation of the tide in the limit $\zeta/H \to 0$ in Section 3.2 in Supporting Information S1.

For the present approximation, we assume that the vertical structure of salinity and velocity are not important to the salt transport and hence use the depth-averaged balances for the subtidal salinity $\bar{s}_0$ and M_2 tidal salinity $\bar{s}_1$. Without loss of generality we assume that the depth-averaged tidal velocity may be written as $\bar{u}_1 = \mathcal{U}_t \cos(\omega t)$. Retaining only the terms essential in this regime, i.e.

$$-\mathcal{U}_r \bar{s}_{0,x} + \langle \mathcal{U}_t \bar{s}_{1,x} \rangle = 0 \tag{A1a}$$

$$\bar{s}_{1,t} - \mathcal{U}_r \bar{s}_{1,x} + \mathcal{U}_t \bar{s}_{0,x} = 0 \tag{A1b}$$

The M_2 salinity is written as $\bar{s}_1 = \Re\left(\left(\bar{\hat{s}}_1^R(x) + i\bar{\hat{s}}_1^I(x)\right)e^{i\omega t}\right)$ with real functions $\bar{\hat{s}}_1^R(x)$ and $\bar{\hat{s}}_1^I(x)$. Using this expression, we obtain three equations: one for the subtidal salinity and two for the real and imaginary parts of the complex M_2 salinity amplitude

$$-\mathcal{U}_r\bar{s}_{0,x} + \frac{1}{2}\mathcal{U}_t\bar{\hat{s}}_{1,x}^R = 0 \tag{A2a}$$

$$-\omega\bar{\hat{s}}_1^I - \mathcal{U}_r\bar{\hat{s}}_{1,x}^R + \mathcal{U}_t\bar{s}_{0,x} = 0 \tag{A2b}$$

$$\omega\bar{\hat{s}}_1^R - \mathcal{U}_r\bar{\hat{s}}_{1,x}^I = 0 \tag{A2c}$$

This system may be written in matrix-vector product form with a vector $\underline{y} = \left[\bar{s}_0, \bar{\hat{s}}_1^R, \bar{\hat{s}}_1^I\right]^T$ as $A\underline{y}_x + B\underline{y} = \underline{0}$ for some matrices A and B. After some rewriting, this can be cast in the form

$$\underline{y}_x = \begin{bmatrix} 0 & 0 & \frac{\omega\mathcal{U}_t}{\mathcal{U}_t^2 - 2\mathcal{U}_r^2} \\ 0 & 0 & \frac{2\omega\mathcal{U}_r}{\mathcal{U}_t^2 - 2\mathcal{U}_r^2} \\ 0 & \frac{\omega}{\mathcal{U}_r} & 0 \end{bmatrix}\underline{y} \tag{A3}$$

Solutions consist of a linear combination of eigenvectors and $e^{\lambda_i x}$ with eigenvalues λ_i $(i = 1, 2, 3)$. Eigenvalues of this matrix equation may be computed easily by hand. Assuming $\mathcal{U}_r^2 < \frac{1}{2}\mathcal{U}_t^2$, the eigenvalues are real and equal to 0, $\frac{\omega}{\sqrt{\frac{1}{2}\mathcal{U}_t^2 - \mathcal{U}_r^2}}$, and $-\frac{\omega}{\sqrt{\frac{1}{2}\mathcal{U}_t^2 - \mathcal{U}_r^2}}$. We may ignore nonnegative eigenvalues as the corresponding eigenfunctions will not satisfy the condition $s \to 0$ for $x \to \infty$. Hence, the only relevant eigenvalue equals

$$\lambda = -\frac{\omega}{\sqrt{\frac{1}{2}\mathcal{U}_t^2 - \mathcal{U}_r^2}} \tag{A4}$$

And the solution reads as

$$\bar{s}_0 = \bar{s}_0(0)e^{\lambda x} \tag{A5a}$$

$$\bar{\hat{s}}_1^R = \bar{s}_0(0)\frac{2\mathcal{U}_r}{\mathcal{U}_t}e^{\lambda x} \tag{A5b}$$

$$\bar{\hat{s}}_1^I = -\bar{s}_0(0)\frac{\sqrt{2}\sqrt{\mathcal{U}_t^2 - 2\mathcal{U}_r^2}}{\mathcal{U}_t}e^{\lambda x} \tag{A5c}$$

where $\bar{s}_0(0)$ is the subtidal salinity at $x = 0$. When $\mathcal{U}_r^2 > \frac{1}{2}\mathcal{U}_t^2$, eigenvalues are complex with zero real part, so that no solutions exist satisfying $s \to 0$ for $x \to \infty$.

There are two apparent problems concerning this simple approximation. First, Figure 3 shows that the along-channel salinity profiles are not at all exponential as implied here. Second, this solution does not satisfy the boundary condition $\bar{s}_{1,x} = 0$ at $x = 0$. These problems may be solved by including an M_4 tidal component and retaining the horizontal dispersive terms in the equations. This is done in Section 3a in Supporting Information S1. It has been checked that the length-scale derived above is a good estimate of the dominant length scale of the solution presented in Supporting Information S1.

Data Availability Statement

The results can be reproduced using the code and input available under iFlow version 3.0 on GitHub (doi:10.5281/zenodo.822394).

Acknowledgments
This research was funded by the Dutch Science Organisation (NWO, Grant ALWSD.2016.015). The 3D numerical model results used in the case study originate from the project "Dispersion mechanisms in the Rhine-Meuse Delta," project 11203735-004, assigned to Deltares by the Dutch Directorate-General for Public Works and Water Management (Dutch: "Rijkswaterstaat"), using the OSR model developed and maintained by Port of Rotterdam.

References

Aristizábal, M. F., & Chant, R. J. (2013). A numerical study of salt fluxes in Delaware Bay Estuary. *Journal of Physical Oceanography*, *43*(8), 1572–1588. https://doi.org/10.1175/jpo-d-12-0124.1

Armi, L. (1986). The hydraulics of two flowing layers with different densities. *Journal of Fluid Mechanics*, *163*, 27–58. https://doi.org/10.1017/s0022112086002197

Bellafiore, D., Ferrarin, C., Maicu, F., Manfè, G., Lorenzetti, G., Umgiesser, G., et al. (2021). Saltwater intrusion in a Mediterranean delta under a changing climate. *Journal of Geophysical Research: Oceans*, *126*, e2020JC016437. https://doi.org/10.1029/2020JC016437

Bowden, K. F. (1965). Horizontal mixing in the sea due to a shearing current. *Journal of Fluid Mechanics*, *21*(1), 83–95. https://doi.org/10.1017/s0022112065000058

Bowen, M. M., & Geyer, W. R. (2003). Salt transport and the time-dependent salt balance of a partially stratified estuary. *Journal of Geophysical Research*, *108*(C5), 3158. https://doi.org/10.1029/2001JC001231

Chatwin, P. C. (1975). On the longitudinal dispersion of passive contaminant in oscillatory flows in tubes. *Journal of Fluid Mechanics*, *71*(3), 513–527. https://doi.org/10.1017/s0022112075002716

Chatwin, P. C. (1976). Some remarks and on the maintenance and of the and salinity distribution and in estuaries. *Estuarine and Coastal Marine Science*, *4*(5), 555–566. https://doi.org/10.1016/0302-3524(76)90030-X

Chatwin, P. C., & Allen, C. M. (1985). Mathematical models of dispersion in rivers and estuaries. *Annual Review of Fluid Mechanics*, *17*(1), 119–149. https://doi.org/10.1146/annurev.fl.17.010185.001003

DeGoede, E. D. (2020). Historical overview of 2D and 3D hydrodynamic modelling of shallow water flows in the Netherlands. *Ocean Dynamics*, *70*(4), 521–539. https://doi.org/10.1007/s10236-019-01336-5

Dijkstra, Y. M., Brouwer, R. L., Schuttelaars, H. M., & Schramkowski, G. P. (2017a). The iFlow modelling framework v2.4. A modular idealized process-based model for flow and transport in estuaries. *Geoscientific Model Development*, *10*(7), 2691–2713. https://doi.org/10.5194/gmd-10-2691-2017

Dijkstra, Y. M., & Schuttelaars, H. M. (2021). A unifying approach to subtidal salt intrusion modeling in tidal estuaries. *Journal of Physical Oceanography*, *51*(1), 147–167. https://doi.org/10.1175/JPO-D-20-0006.1

Dijkstra, Y. M., Schuttelaars, H. M., & Burchard, H. (2017b). Generation of exchange flows in estuaries by tidal and gravitational eddy viscosity-shear covariance (ESCO). *Journal of Geophysical Research: Oceans*, *122*, 4217–4237. https://doi.org/10.1002/2016JC012379

Dronkers, J., & van de Kreeke, J. (1986). Experimental determination of salt intrusion mechanisms in the Volkerak estuary. *Netherlands Journal of Sea Research*, *20*(1), 1–19. https://doi.org/10.1016/0077-7579(86)90056-6

Dyer, K. (1974). The salt balance in stratified estuaries. *Estuarine and Coastal Marine Science*, *2*(3), 273–281. https://doi.org/10.1016/0302-3524(74)90017-6

Fischer, H. B. (1972). Mass-transport mechanisms in partially stratified estuaries. *Journal of Fluid Mechanics*, *53*(4), 671–687. https://doi.org/10.1017/s0022112072000412

Fischer, H. B. (1976). Mixing and dispersion in estuaries. *Annual Review of Fluid Mechanics*, *8*(1), 107–133. https://doi.org/10.1146/annurev.fl.08.010176.000543

Fischer, H. B., List, E. J., Koh, R. C. Y., & Imberger, J. (1979). *Mixing in inland and coastal waters*. Academic Press.

Garcia, A. M. P., Geyer, W. R., & Randall, N. (2021). Exchange flows in tributary creeks enhance dispersion by tidal trapping. *Estuaries and Coasts*, *45*(2), 363–381. https://doi.org/10.1007/s12237-021-00969-4

Geyer, W. R. (2010). Estuarine salinity structure and circulation. In A. Valle-Levinson (Ed.), *Estuarine salinity structure and circulation*. *Contemporary issues in estuarine physics* (pp. 12–26). Cambridge University Press. https://doi.org/10.1017/cbo9780511676567.003

Geyer, W. R., & Farmer, D. M. (1989). Tide-induced variation of the dynamics of a salt wedge estuary. *Journal of Physical Oceanography*, *19*(8), 1060–1072. https://doi.org/10.1175/1520-0485(1989)019<1060:tivotd>2.0.co;2

Geyer, W. R., & MacCready, P. (2014). The estuarine circulation. *Annual Review of Fluid Mechanics*, *46*(1), 175–197. https://doi.org/10.1146/annurev-fluid-010313-141302

Geyer, W. R., & Ralston, D. (2011). The dynamics of strongly stratified estuaries. In *Treatise on estuarine and coastal science* (pp. 37–51). Elsevier. https://doi.org/10.1016/b978-0-12-374711-2.00206-0

Geyer, W. R., & Ralston, D. K. (2015). Estuarine frontogenesis. *Journal of Physical Oceanography*, *45*(2), 546–561. https://doi.org/10.1175/jpo-d-14-0082.1

Guha, A., & Lawrence, G. A. (2013). Estuary classification revisited. *Journal of Physical Oceanography*, *43*(8), 1566–1571. https://doi.org/10.1175/jpo-d-12-0129.1

Hansen, D. V., & Rattray, M. (1965). Gravitational circulation in straits and estuaries. *Journal of Marine Research*, *23*, 104–122.

Holley, E. R., Harleman, D. R. F., & Fischer, H. B. (1970). Dispersion in homogeneous estuary flow. *Journal of the Hydraulics Division*, *96*(8), 1691–1709. https://doi.org/10.1061/jyceaj.0002626

Hughes, F. W., & Rattray, M. (1980). Salt flux and mixing in the Columbia River estuary. *Estuarine and Coastal Marine Science*, *10*(5), 479–493. https://doi.org/10.1016/s0302-3524(80)80070-3

Jay, D. A., & Smith, J. D. (1990). Residual circulation in shallow estuaries 1. Highly stratified, narrow estuaries. *Journal of Geophysical Research*, *95*(C1), 711–731. https://doi.org/10.1029/JC095iC01p00711

Kranenburg, C. (1986). A time scale for long-term salt intrusion in well-mixed estuaries. *Journal of Physical Oceanography*, *16*(7), 1329–1331. https://doi.org/10.1175/1520-0485(1986)016<1329:atsflt>2.0.co;2

Kranenburg, W. M., & Van der Kaaij, T. (2019). Dispersiemechanismen in de Rijn-Maasmonding. Verkenning van de verhouding tussen zouttransportprocessen middels zoutfluxdecompositie (Tech. Rep. No. 11203735-004) (in Dutch). Deltares. Retrieved from http://publications.deltares.nl/11203735_004.pdf

Kranenburg, W. M., Van der Kaaij, T., & Nolte, A. J. (2015). Evaluatie van het OSR-model voorzoutindringing in de Rijn-Maasmonding (II) (Tech. Rep. No. 1220070-000) (in Dutch). Deltares. Retrieved from http://publications.deltares.nl/1220070_000b.pdf

Kranenburg, W. M., Van der Kaaij, T., Tiessen, M., Friocourt, Y., & Blaas, M. (2022). Salt intrusion in the Rhine Meuse Delta: Estuarine circulation, tidal dispersion or surge effect? In *Proceedings of the 39th IAHR World Congress 19–24 June 2022* (pp. 5601–5608). https://doi.org/10.3850/IAHR-39WC2521716X20221058

Kranenburg, W. M., Van der Kaaij, T., Van den Boogaard, H. F. P., Uittenbogaard, R. E., & Dijkstra, Y. M. (2016). Unraveling salt fluxes: A tool to determine flux components and dispersion rates from 3D models. In *Era of global change—Proceedings of the 4th European Congress of the International Association of Hydroenvironment Engineering and Research (IAHR 2016)* (pp. 1010–1017). https://doi.org/10.1201/b21902-167

Lange, X., & Burchard, H. (2019). The relative importance of wind straining and gravitational forcing in driving exchange flows in tidally energetic estuaries. *Journal of Physical Oceanography*, *49*(3), 723–736. https://doi.org/10.1175/jpo-d-18-0014.1

Larsen, L. H. (1977). Dispersion of a passive contaminant in oscillatory fluid flows. *Journal of Physical Oceanography*, *7*(6), 928–931. https://doi.org/10.1175/1520-0485(1977)007<0928:doapci>2.0.co;2

Lerczak, J. A., Geyer, W. R., & Chant, R. J. (2006). Mechanisms driving the time-dependent salt flux in a partially stratified estuary. *Journal of Physical Oceanography*, *36*(12), 2296–2311. https://doi.org/10.1175/JPO2959.1

MacCready, P. (2004). Toward a unified theory of tidally-averaged estuarine salinity structure. *Estuaries*, *27*(4), 561–570. https://doi.org/10.1007/BF02907644

MacVean, L. J., & Stacey, M. T. (2011). Estuarine dispersion from tidal trapping: A new analytical framework. *Estuaries and Coasts*, *34*(1), 45–59. https://doi.org/10.1007/s12237-010-9298-x

McCarthy, R. K. (1993). Residual currents in tidally dominated, well-mixed estuaries. *Tellus*, *45A*(4), 325–340. https://doi.org/10.1034/j.1600-0870.1993.00007.x

Okubo, A. (1973). Effect of shoreline irregularities on streamwise dispersion in estuaries and other embayments. *Netherlands Journal of Sea Research*, *6*(1–2), 213–224. https://doi.org/10.1016/0077-7579(73)90014-8

Ou, H.-W., Dong, C.-M., & Chen, D. (2000). On the tide-induced property flux: Can it be locally counter gradient? *Journal of Physical Oceanography*, *30*(6), 1472–1477. https://doi.org/10.1175/1520-0485(2000)030<1472:ottipf>2.0.co;2

Pacanowski, R. C., & Philander, S. G. H. (1981). Parameterization of vertical mixing in numerical models of tropical oceans. *Journal of Physical Oceanography*, *11*(11), 1443–1451. https://doi.org/10.1175/1520-0485(1981)011<1443:povmin>2.0.co;2

Ralston, D. K., Geyer, W. R., & Lerczak, J. A. (2008). Subtidal salinity and velocity in the Hudson River estuary: Observations and modelling. *Journal of Physical Oceanography*, *38*(4), 753–770. https://doi.org/10.1175/2007jpo3808.1

Schijf, J. B., & Schönfeld, J. C. (1953). Theoretical considerations on the motion of salt and fresh water. In *Proceedings: Minnesota International Hydraulic Convention*.

Simpson, J. H., Brown, J., Matthews, J., & Allen, G. (1990). Tidal straining, density currents, and stirring in the control of estuarine stratification. *Estuaries*, *13*(2), 125–132. https://doi.org/10.2307/1351581

Souza, A. J. (2013). On the use of the Stokes number to explain frictional tidal dynamics and water column structure in shelf seas. *Ocean Science*, *9*(2), 391–398. https://doi.org/10.5194/os-9-391-2013

Wang, T., Geyer, W. R., Engel, P., Jiang, W., & Feng, S. (2015). Mechanisms of tidal oscillatory salt transport in a partially stratified estuary. *Journal of Physical Oceanography*, *45*(11), 2773–2789. https://doi.org/10.1175/jpo-d-15-0031.1

Watson, E. J. (1983). Diffusion in oscillatory pipe flow. *Journal of Fluid Mechanics*, *133*, 233–244. https://doi.org/10.1017/s0022112083001883

Wei, X., Schramkowski, G. P., & Schuttelaars, H. M. (2016). Salt dynamics in well-mixed estuaries: Importance of advection by tides. *Journal of Physical Oceanography*, *46*(5), 1457–1475. https://doi.org/10.1175/jpo-d-15-0045.1

Wei, X., Schuttelaars, H. M., Williams, M. E., Brown, J. M., Thorne, P. D., & Amoudry, L. O. (2021). Unravelling interactions between asymmetric tidal turbulence, residual circulation and salinity dynamics in short, periodically weakly stratified estuaries. *Journal of Physical Oceanography*, *51*(5), 1395–1416. https://doi.org/10.1175/jpo-d-20-0146.1